Engineering Structures 305 (2024) 117718

Contents lists available at ScienceDirect

Engineering Structures

journal homepage: www.elsevier.com/locate/engstruct

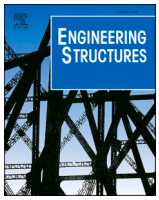

Preliminary experimental tests of a novel friction damper for seismic retrofit of RC precast structures

Eleonora Grossi *, Alessandra Aprile, Matteo Zerbin, Paolo Livieri

Engineering Department, University of Ferrara, via Saragat 1, 44122 Ferrara, Italy

ARTICLE INFO

Keywords:
RC precast structures
Rotational friction damper
Beam-to-column connections
Cyclic tests
Experimental tests

ABSTRACT

Precast RC structures have been widely adopted for industrial and commercial buildings since the '60 s in the most developed countries. For this structural typology, connections between structural elements set a crucial point in the presence of lateral loads, such as earthquakes, since the deficiency, or lacking, of connection elements is the main responsible for their structural collapse. This paper shows the preliminary mechanical testing of an innovative damping device conceived to be installed in beam-to-column joints of precast RC structures, with a bidirectional dissipative potential due to its geometry. This new Bidirectional Rotation Friction Damper (BRFD) has been designed and optimised after a tribological campaign, which led to the selection of the two different friction interfaces investigated in this work. The mechanical tests have been performed considering the guidelines of EN15129 and the previous tribological investigation findings, showing the influence of sliding frequency and bolt torque increment on the steadiness of the BRFD hysteresis cycle.

1. Introduction

In the context of the seismic rehabilitation of existing buildings, passive control techniques based on energy dissipation devices have proved to be a very efficient solution, being much cheaper if compared to traditional retrofit techniques [1,2], and able to prevent damage to structural elements [3]. Most common and simple dissipation devices are of the hysteretic type, based on yielding or friction properties of metallic materials.

Friction Dampers (FD) have been tested and applied starting from the early Pall and Marsh's works in the '80 s [4] and since then, FDs have been declined in several typologies, being the focus of an increasing number of studies [5]. Jaisee et. al [5] highlighted how FDs are an effective tool for retrofitting thanks to the consistent and rectangular-shaped hysteresis loop, which maximises the energy dissipation capacity, being a reliable solution. In fact, their performance is not generally influenced by the loading amplitude, frequency, and number of cycles, consequently, FDs can perform under several and subsequent seismic events without a significant decrement in terms of dissipation capacity. However, FDs exhibit some limitations connected to the friction phenomena itself, like the stick-slip mechanism, which is strictly related to the selected friction interface, and bolts pre-tension, which can affect the stability and consistency of the hysteresis loops. At the same time, some limitations are also connected to the structural layout of the devices, like the re-centring capacity: traditional FDs do not assure it, however, re-centring layouts affect the rectangular-shape hysteresis loop, decrementing the damping capacity. The listed limitations underline the need for more research focused on both tribological and layout aspects, also considering the application field and the FDs installation joints.

Considering the civil engineering field, precast RC structures designed for gravity loads only are one of the most vulnerable structural systems under seismic action. The early 2000 state-of-the-art FIB report on the seismic design of precast RC building structures [6] shows the crucial relationship between structural joints and the seismic response of such buildings. All the collapsed structures had poor or lacking connections between elements, while structures with efficient joints showed optimal performances and correct development and placement of plastic hinges [7]. The topic of precast RC structures vulnerability is particularly sensitive in the Southern European territories [8–10], where the late update of both the seismic regulations and the national seismic hazards maps is one of the main responsible for the high number of seismically inadequate precast RC buildings.

FDs are typically installed on the frame braces with a strong impact on the existing structural system, often requiring additional supporting elements and decreasing the usable surface area due to their dimensions

* Corresponding author.
E-mail address: eleonora.grossi@unife.it (E. Grossi).

https://doi.org/10.1016/j.engstruct.2024.117718
Received 4 September 2023; Received in revised form 2 February 2024; Accepted 18 February 2024
Available online 1 March 2024

[11–16]. The need for structural connection improvement and minimally invasive energy dissipation devices brings to the concept of dissipative beam-to-column joints, meeting both requirements in one device.

Several studies have been conducted on steel frames [17–19], as well as on precast RC frames [20–28], to develop devices performing as beam-to-column connections and dampers simultaneously. Concerning the devices designed for precast RC structures retrofit, most studies focused on friction-based solutions. Eldin et al. [20] presented a FD with a movable geometry that performs as a beam-to-column connection of precast post-tensioned RC structures and energy dissipation arises thanks to the linear sliding of elements. Huang et al. [21] suggested the adoption of a bolted web FD and added grooves to the friction pads to increase the stiffness of the system and the associated dissipated energy. Valente [22] conducted studies on a Rotational Friction Damper (RFD) applied in the beam-to-column corner that dissipates energy thanks to the subsequent opening and closing of the gap between these structural elements during the seismic actions. Colajanni et al. [23] conducted additional studies by integrating the solution suggested by Valente [22] with a bolted web FD to increase the damping capacity of the system. Martinelli and Mulas [24] revised the configuration of beam-to-column connections by connecting an RFD with two orthogonal steel beams. Such a solution has been updated by Belleri et al. [25] by adding a re-centring element. Concerning the studies focused on devices based on yielding of steel elements, Pollini et al. [26] and Huang et al. [27] presented devices based on the yielding of steel tubes and added fibre wrapping and concrete filling, respectively, to avoid instabilities during the yielding process. A last promising solution has been studied in the work of Bressanelli et al. [28], in which a crescent moon steel element has been designed and optimised to connect beam and column.

These studies have generally highlighted a good structural performance of the proposed devices, in terms of both energy dissipation and base shear reduction. However, such devices are typically installed in beam-to-column joints of main frames and the damping force acts within the plane of main frames. Thus, orthogonal main frames with added devices are required to get energy dissipation in both directions, as required by the seismic action.

This paper shows the early mechanical testing of an innovative damping device, conceived to be installed in beam-to-column joints of precast RC structures, to assess the selected friction interfaces on the real-scale device. The presented device is able to simultaneously dissipate energy along the in-plane and out-of-plane directions of the installation main frame. Starting conceptually from a simple RFD, and using a movable plate geometry, a Bidirectional Rotational Friction Damper (BRFD) is created producing a relevant damping effect in two main directions.

Section 2 describes the BRFD structural layout and briefly highlights the findings of a preliminary tribological investigation performed at the Metallurgy Laboratory (Engineering Department, University of Ferrara, Italy) [29,30] defining the investigated friction interfaces. Section 3 shows the real-scale BRFD prototype, the experimental setup, and the adopted testing protocols, considering the guidelines of EN15129 [31] during the early mechanical investigation carried out at the Structural Integrity Laboratory (Engineering Department, University of Ferrara, Italy), Section 4 shows the results and comments of the mechanical tests, while a final Section 5 collects the main remarks.

2. BRFD prototype and structural layout

The BRFD is made by assembling layered steel plates whose contact surfaces dissipate energy by friction, as shown in the axonometric view of Fig. 1(a). The BRFD is connected to the main frame in the beam-to-column joints with an inclination angle of about 45° from the longitudinal beam axis (see Fig. 1(b)), depending on the available space. To permit the BRFD to behave bidirectionally, the local *xy* plane and global *XY* plane form an angle of 45° (see the scheme in Fig. 1(b)). Moreover, to allow the BRFD longitudinal (local *x*-axis) deformations, the end of the elements that connect the BRFD to the existing beam and column are hinged, allowing rotation around the global *Y*-axis only.

The main elements of the BRFD are core plates and core connection plates, which are kept coupled by four preload stud bolts. The geometry and mechanical properties of these elements highly influence the BRFD activation force and initial stiffness. Belleville spring washers are used to avoid the loss of bolt tension during the cycling excitations, as suggested by several studies (among the others see [32,33]), adopting a two-in-series configuration for each stud bolt.

When the BRFD is activated, the ends of the core central and side plates rotate around the preload stud bolts, dissipating energy thanks to the friction generated by the contact of the plates (see the red area of Fig. 2). At the top and the bottom of the BRFD, two guides with slotted

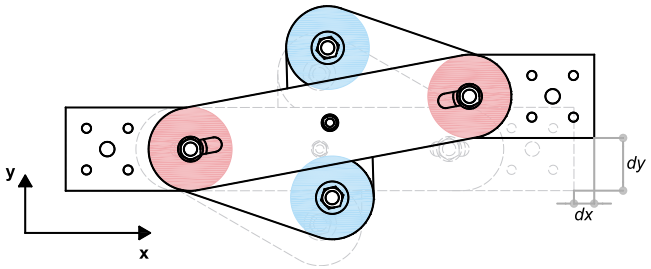

Fig. 2. BRFD bidirectional deformed shape: combination of longitudinal and transversal components.

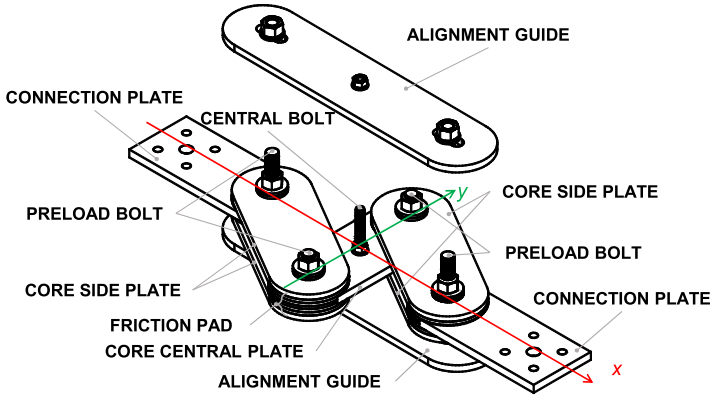

(a)

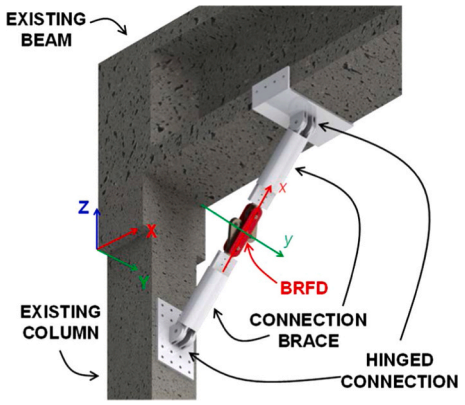

(b)

Fig. 1. Axonometric view of (a) the BRFD and (b) the frame connection scheme.

holes keep the preload stud bolts of core connection plates lined-up with the central stud bolt to maintain the displacements under control and to set a displacement limit according to EN 15129 limitations [31]. The movable geometry of the BRFD allows the performance of two-component displacement: the first component is longitudinal (*dx*) and the second is transversal (*dy*), as shown in Fig. 2. As a result, the BRFD activation force has two components: longitudinal ($F_{act,x}$) and transversal ($F_{act,y}$). Moreover, when the BRFD is subjected to longitudinal displacement the energy dissipation occurs in correspondence with the blue area (see Fig. 2, *dx* displacement), while for transversal displacements the energy dissipation occurs in correspondence with the red area (see Fig. 2, *dy* displacement). This decoupled behaviour is extremely important because allows to describe the BRFD with two independent displacement components.

It is worth noting that to achieve the deformed shape of Fig. 2, the ends of the core connection plates (see Fig. 1(a)) have to be fixed, preventing their relative rotation when the BRFD is subsequently lengthened and shortened. In fact, when the BRFD is moving, only the core central and core side plates rotate, while the alignment guides avoid the misalignment of core elements.

When the BRFDs are placed inside a precast RC frame, the static scheme of the columns changes from cantilever (Figs. 3(a) and 3(c)) into fixed (Figs. 3(b) and 3(d)), leading to an increment of structural stiffness in both in-plane and out-of-plane frame's directions (see Fig. 3). However, after the BRFDs start sliding, the columns return to behave as cantilever and their deformed shape in the in-plane (*X*) and out-of-plane (*Y*) directions allows the subsequent opening and closure of the beam-to-column joint.

When the BRFD is activated, its corresponding activation forces are concentrated on both beams and columns' connection points (see Fig. 1(b)), and, in addition, beams might slip on the columns' top section if beam-to-column connections are poor or lacking (like in many pre-seismic code constructions). For these reasons, the structural design of the BRFD is driven by respecting, under any circumstance, the following main conditions:

1. During the seismic motion, if a mechanical fastening is not installed, RC beams and columns cannot slide on each other.
2. Shear and flexural seismic demand of RC beams and columns cannot exceed their capacity.

To perform the mechanical testing, the design of the BRFD prototype first requested the selection of proper coupling surfaces able to develop a reliable and steady friction coefficient μ. A preliminary tribological investigation has been performed at the Metallurgy Laboratory (Engineering Department, University of Ferrara, Italy) [29,30], to compare the effects on μ steadiness of different surfaces finishing and treatments. The tribological tests have been set up to reproduce the BRFD effective behaviour and it has been observed that the overall μ steadiness increases significantly after performing running-in stages. Of all the investigated surfaces, the better-performing couplings were nickelled steel vs. nickelled steel (NN) and nickelled steel vs. bronze (NB). These two configurations have been selected to manufacture the BRFD prototype and have been investigated to assess the influence of bolt axial preload and sliding velocity on the BRFD overall behaviour. The BRFD prototype in here investigated has been designed following the results of an optimisation analysis carried out on a real case study of a precast RC structure retrofitting [34,35]. According to the obtained findings, the better-performing devices required activation forces around 10–20 kN and maximum displacements of 40 mm.

3. Experimental setup and testing protocol

The mechanical tests have been performed at the Structural Integrity Laboratory (Engineering Department, University of Ferrara, Italy) using an MTS servo-hydraulic testing machine with a maximum load capacity of 250 kN testing machine and control system as shown in Fig. 4(a). The experimental layout of the BRFD prototype (see Fig. 5(a)) slightly differs from the layout of Fig. 1(a). Two additional steel guides (the experimental setup guides of Fig. 5(a)) with slotted holes have been added to exclude rotations at the ends of the connection plates and, at the same time, to ensure a hinged connection to the actuator (see Fig. 5(a)). In fact, the experimental setup guides exclude bending moment at the device ends, for the safety of the testing machine, by using the bolts couples within the slotted holes (see Fig. 5(a)). To reduce possible friction between stud bolts and the slotted holes of the additional guide, lubricated bushes were introduced for each bolt. To assess the

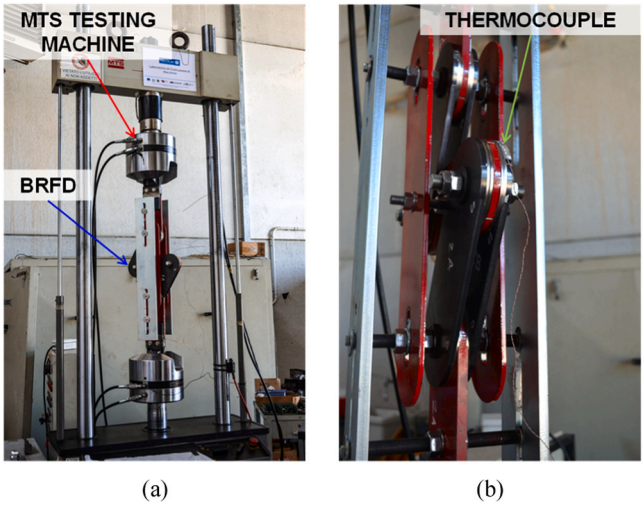

Fig. 4. Experimental setup a) general overview and b) detail of thermocouples connection.

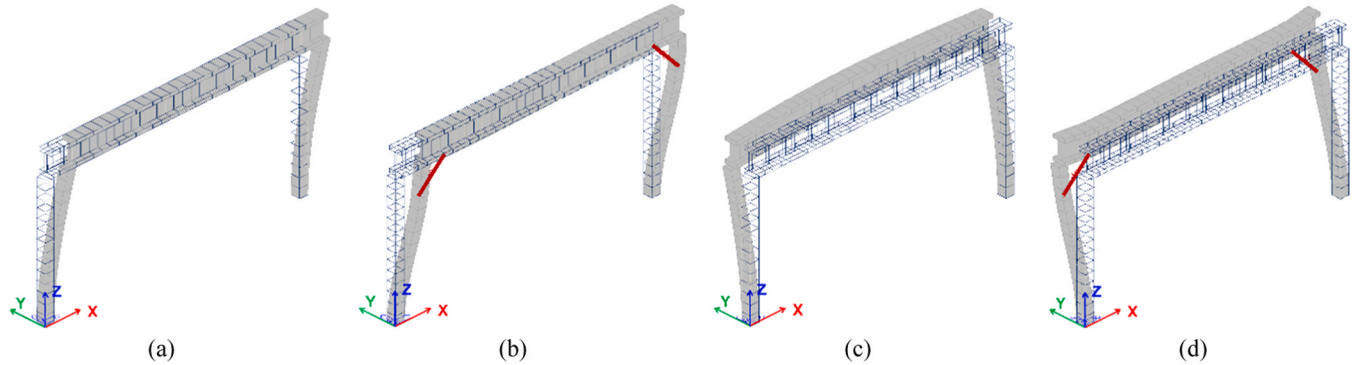

Fig. 3. Frame deformation in *X* direction (a) without and (b) with BRFD, and in *Y* direction (c) without and (d) with BRFD.

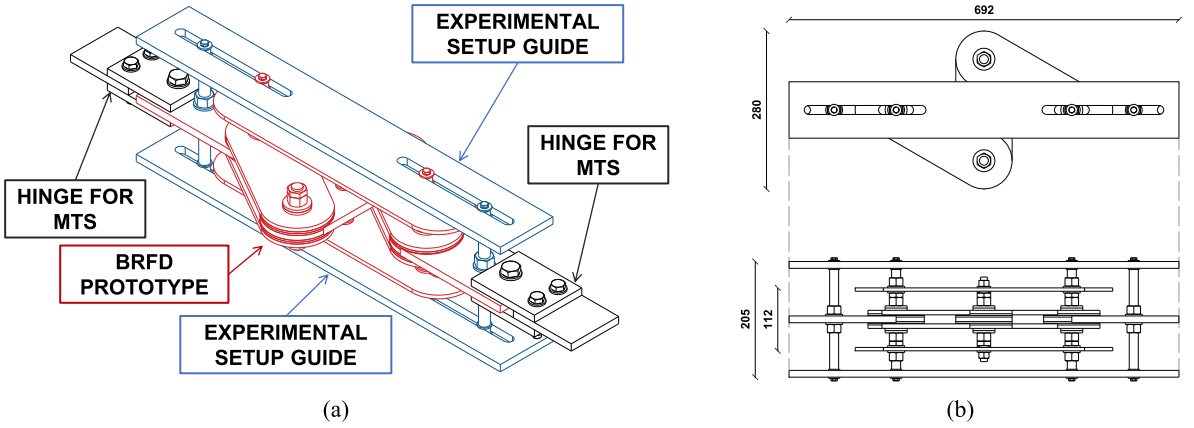

Fig. 5. BRFD prototype drawings: a) axonometric view with details and b) top and side view. Dimensions in mm.

experimental setup, some cycles were performed on the prototype without preload of the stud bolts to measure the influence the additional guides on the recorded forces. The obtained forces resulted lower than 5% of the forces recorded on the prototype with preload of the stud bolts. At the early stage of the mechanical testing, the behaviour of the BRFD has been investigated only in the longitudinal direction, despite the bidirectional potential, focusing on the behaviour of the selected friction interfaces.

The prototype has been manufactured using S355JR structural steel [36], using four M16 class 8.8 [37] preload stud bolts and one M12 class 8.8 [37] central stud bolts. Two additional M16 class 8.8 [37] stud bolts have been added to the prototype to connect the two additional steel guides. As showed in Fig. 5(b), the overall dimension of the prototype is 70x30x20 cm. Nuts have been closed using a FERVI 0803/S210 manual torque wrench (FERVI SpA, Modena, Italy) to ensure the application of constant tension to the stud bolts.

During the test execution, forces and displacements of the device have been recorded by means of the MTS internal measurement system. The prototype was equipped with several sensors to detect the temperature increment in correspondence with the dissipating areas. K-thermocouples connected to a TC-08 thermocouple data logger (Pico Technology, St Neots, United Kingdom) were placed close to the BRFD's friction interface to measure the temperature increment in the proximity of the working area, assessing the amount and the effects of the temperature increment on the BRFD behaviour (see Fig. 4(b) for the detailed view).

The testing protocols were defined according to EN15129 [31], which prescribes, for friction damper devices, quasi-static incremental displacements performing at least five cycles at 25%, five cycles at 50% and ten cycles at 100% of the device maximum allowable displacement. However, several studies (among the others see [33,38,39]) show how the performance of friction devices can be significantly influenced by the sliding velocity and the variation of bolt axial load. In addition, the tribological investigation previously performed for the BRFD development highlighted how the overall μ steadiness increases significantly after performing running-in stages [29,30].

Three different frequencies have been considered in defining the testing protocols: 0.05 Hz has been selected to perform the quasi-static tests while 0.50 and 1.00 Hz have been selected to perform the dynamic tests (F1, F2 and F3 tags respectively). Concerning the torque of the stud bolts, three different levels have been considered: 40, 60 and 100 Nm (T1, T2 and T3 tags respectively), which corresponds to 20%, 30% and 50% of the maximum M16 [37] allowable torque. Concerning the displacement amplitudes, a maximum allowable displacement of $\pm$ 40 mm has been used to define the testing protocols. However, due to the testing equipment capacity limitation, the maximum displacement had to be decreased when incrementing the frequency, consequently, three different target displacements have been considered: $\pm$ 40, $\pm$ 20 and $\pm$ 10 mm (A1, A2 and A3 tags at frequencies F1, F2 and F3 respectively).

The testing procedure has been divided into three different steps. The first one is the running-in (RI) tests (see Table 1), which are performed to properly develop a conformal contact between the surfaces of friction interface. The second one is the Group 1 (G1) tests (see Table 2), which are performed with fixed frequency and incrementing displacement amplitude, resembling the EN15129 [31] requested procedure. The final one is the Group 2 (G2) tests (see Table 3), which are performed with fixed displacement amplitude and incrementing frequency, focusing on the sliding velocity influence.

All the tests have been performed for both NN and NB configurations. RI tests considered only T1 torque, G1 tests considered T1, T2 and T3 torque, and G2 tests considered only T3 torque. All the tests have been conducted at room temperature, waiting for specimens to cool off if the increment of temperature at the end of a previous test exceeded 10% of the room temperature.

4. Results and discussion

The experimental results of RI, G1 and G2 tests are here presented using Matlab as post-processing software [40].

The BRFD is a device based on friction, consequently during the RI tests the recorded hysteresis cycle registers the evolution of the Fig. 6 scheme: when the BRFD is subjected to n-cycles between $\pm d_{max}$, the hysteresis area increments until the development of a conformal contact between the sliding surfaces, reaching a stable behaviour. More precisely, when the surfaces of a friction interface start sliding, wear debris starts to accumulate forming a layer. The more compact this layer is, the more stable and smooth the coefficient of friction is [29].

The first cycle is defined by the forces $F^{+}_{act,1}$, the positive force developed at the first sliding, $F_{act,1}{}^{-}$, the negative force developed at zero-displacement, $F^{+}_{max,1}$, the force developed at the displacement $+ d_{max}$, and $F_{max,1}{}^{-}$, the force developed at the displacement $- d_{max}$. Starting from the second cycle, each i-cycle's loop is defined by the forces $F^{+}_{act,i}$, the positive force developed at zero-displacement, $F_{act,i}{}^{-}$, the negative force developed at zero-displacement), $F^{+}_{max,i}$, the force developed at the displacement $+ d_{max}$, and $F_{max,i}{}^{-}$, the force developed at the displacement $- d_{max}$.

To define the shape of the hysteresis cycle after the development of

Table 1
Running-in test procedure.

Test group code	Fixed frequency	Fixed amplitude	Torque	Total duration
RI	0.50 Hz	$\pm$ 20 mm	40 Nm	300 s

Table 2
Group 1 test procedure.

Test group code	Fixed frequency	Increment sequence	Torque level	Total duration
G1-F1	0.05 Hz	± 10 mm (25% A1) - 180 s ± 20 mm (50% A1) - 180 s ± 40 mm (100% A1) - 180 s	40 Nm 60 Nm 100 Nm	540 s
G1-F2	0.50 Hz	± 5 mm (25% A2) - 60 s ± 10 mm (50% A2) - 60 s ± 20 mm (100% A2) - 60 s	40 Nm 60 Nm 100 Nm	180 s
G1-F3	1.00 Hz	± 2.5 mm (25% A3) - 60 s ± 5 mm (50% A3) - 60 s ± 10 mm (100% A3) - 60 s	40 Nm 60 Nm 100 Nm	180 s

Table 3
Group 2 test procedure.

Test group code	Fixed amplitude	Increment sequence	Torque	Total duration
G2	± 10 mm	0.05 Hz - 120 s 0.10 Hz - 60 s 0.15 Hz - 60 s 0.20 Hz - 30 s 0.25 Hz - 30 s 0.50 Hz - 30 s 0.75 Hz - 30 s 1.00 Hz - 30 s	100 Nm	390 s

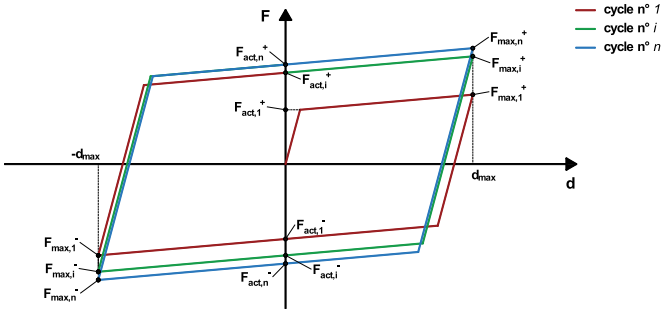

Fig. 6. Hysteresis cycle evolution scheme.

the friction interface coupling (i.e. when it reaches a steady behaviour), it is important to identify the transition time t_{tr}, defined as the time needed to reach a steady behaviour. For each i-cycle ($i = 1,.., n$) a mean activation force $F_{act,i}$ and a maximum force $F_{max,i}$ are calculated respectively as the average value between positive and negative forces developed at zero-displacement, and the average value between the force developed at the displacement $\pm d_{max}$ (see Eq. (1)).

$$F_{act,i} = \frac{\left|F_{act,i}^{+}\right| + \left|F_{act,i}^{-}\right|}{2} \quad ; \quad F_{\max,i} = \frac{\left|F_{\max,i}^{+}\right| + \left|F_{\max,i}^{-}\right|}{2} \quad i = 1, \ldots, n \tag{1}$$

Subsequently, it is evaluated the percentage difference between $F_{act,i}$ and $F_{act,i-1}$, and between $F_{max,i}$ and $F_{max,i-1}$, as for Eq. (2). The number of cycles n_s needed to reach a steady behaviour is evaluated as the bigger between the number of cycles needed to reach $dF_{act,i} < 5\%$ and the number of cycles needed to reach $dF_{max,i} < 5\%$.

$$dF_{act,i} = \left|\frac{F_{act,i} - F_{act,i-1}}{F_{act,i}}\right| \quad dF_{\max,i} = \left|\frac{F_{\max,i} - F_{\max,i-1}}{F_{\max,i}}\right| \quad i = 2, \ldots, n \tag{2}$$

RI tests are performed with a fixed frequency f, consequently the transition time t_{tr} is defined as the ratio between n_s and f (see Eq. (3)). The mean activation force $F_{act,s}$ and maximum force $F_{max,s}$ for the steady hysteresis cycles are evaluated as the average value of all $F_{act,i}$ and $F_{max,i}$ for i varying between n_s and the total number of cycles n (see Eq. (4)).

$$t_{tr} = \frac{1}{f} n_s \tag{3}$$

$$F_{act,s} = \frac{\sum_{i=n_s}^{n} F_{act,i}}{n - n_s + 1} \quad ; \quad F_{\max,s} = \frac{\sum_{i=n_s}^{n} F_{\max,i}}{n - n_s + 1} \tag{4}$$

During G1 and G2 tests, the steady behaviour is considered reached, consequently, the mean values $F_{act,s}$ and $F_{max,s}$ are directly evaluated as the average value of all $F_{act,i}$ and $F_{max,i}$ for i varying between 1 and the total number of cycles n.

4.1. Running-in tests (RI)

Figs. 7(a) and 7(b) show RI test results, for NN and NB configuration respectively, in terms of hysteresis cycles as a force-displacement relationship. The difference between NN and NB hysteresis cycles is highly remarkable, both in terms of overall shape and values. NN has an initial rectangular-shaped hysteresis cycle with $F_{act,1}$ value of 2.99 kN. Once the conformal contact between the sliding surfaces is properly developed, NN exhibits a rectangular-shaped hysteresis cycle with an evident hardening effect due to the stick-slip mechanism, with $F_{act,s}$ value of 7.66 kN. NB has an initial rectangular-shaped hysteresis cycle with a slight hardening effect due to the stick-slip mechanism and $F_{act,1}$ value of 2.06 kN. Once the conformal contact between the sliding surfaces is properly developed, NB maintains the rectangular-shaped hysteresis cycle with $F_{act,s}$ value of 3.03 kN.

Figs. 8(a) and 8(b) show RI test results, for NN and NB configuration respectively, in terms of force-time relationship. The orange dashed line highlights the trend of $F_{act,i}$ values, and the blue dashed line highlights the $F_{act,s}$ values. The difference between NN and NB both in terms of overall shape and values is here confirmed. NN force increases rapidly from around 3 kN to 11 kN then decreases slowly and stabilises around 8 kN, registering a transition time t_{tr} of 230 s (n_s equal 115). NB force increases slowly from around 2 kN and stabilises around 3 kN, registering a t_{tr} value of 198 s (n_s equal 99).

Table 4 lists the main results of RI tests in terms of initial activation force $F_{act,1}$, steady activation force $F_{act,s}$, percentage increment between initial and steady activation force ΔF_{act}, coefficient of variation of the overall recorded forces cv_{Fact} and the steady behaviour $cv_{Fact,s}$, transition time t_{tr}, steadiness cycle number n_s and temperature increment ΔT over the initial room temperature. NN configuration exhibits a higher activation force increment (156%), a higher overall coefficient of variation (20%), a higher steady coefficient of variation (6%), a higher transition time (230 s) and a higher temperature increment (32.8 °C). On the contrary, NB configuration exhibits a lower force increment (47%), a lower overall coefficient of variation (9%), a lower steady coefficient of variation (2%), a lower transition time (130 s) and a lower temperature increment (10.7 °C). As a result, at the end of RI tests, both NN and NB configurations develop a conformal contact between the sliding surfaces reaching a steady behaviour; however, NB reached it more quickly and efficiently than NN.

It is worth noting that the difference between NN and NB configurations is mainly caused by the different friction interfaces adopted, confirming the findings of the tribological investigations [29,30]. During the running-in stages, nickelled steel vs. nickelled steel coupling (NN) registered higher μ values than nickelled steel vs. bronze coupling (NB), confirming the higher force values and transition time registered

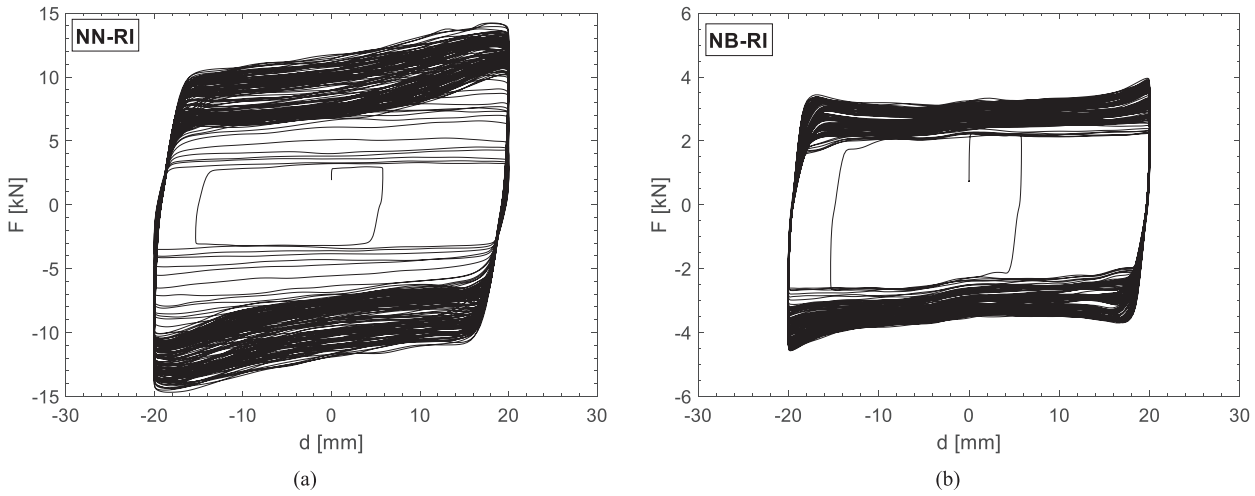

Fig. 7. RI tests hysteresis cycles of a) NN and b) NB configurations.

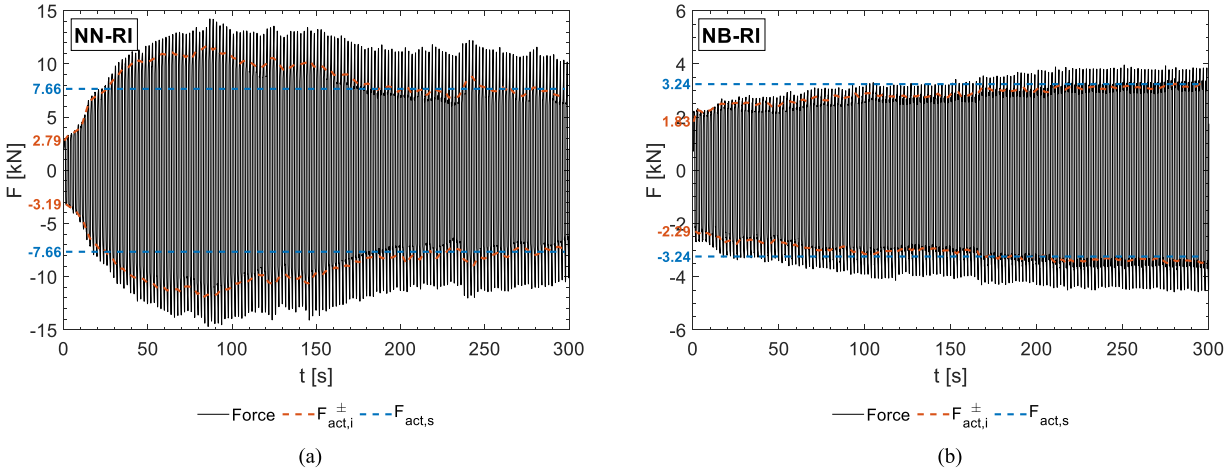

Fig. 8. RI tests registered force for a) NN and b) NB configurations.

Table 4
RI tests main results.

Configuration	$F_{act,1}$ [kN]	$F_{act,s}$ [kN]	ΔF_{act} [%]	cv_{Fact} [%]	$cv_{Fact,s}$ [%]	t_{tr} [s]	n_s	ΔT [°C]
NN	2.99	7.66	156	20	6	230	115	32.8
NB	2.06	3.03	47	9	2	198	99	10.7

by NN than the NB configuration.

4.2. Group 1 tests (G1)

Figs. 9 and 10 show G1 test results, for NN and NB configuration respectively, in terms of hysteresis cycles as a force-displacement relationship for F1, F2 and F3 sliding frequencies.

NN configuration exhibits a rectangular-shaped hysteresis cycle with an evident hardening effect due to the stick-slip mechanism also after the RI tests, resulting in higher force values when reaching higher displacement amplitude. NN configuration exhibits higher values during the tests performed with lower sliding frequencies, with an average force decrement of 55% from F1 to F3. Concerning the effects of the different torque levels, the NN configuration registers higher sliding force values during the tests performed with higher torque values, with an average sliding force increment of 22% from T1 to T3. However, it is worth noting that this difference decreases as the sliding frequency increases.

NB configuration exhibits a rectangular-shaped hysteresis cycle with a slight hardening effect due to the stick-slip mechanism also after the RI tests, resulting in almost equal force values when reaching higher displacement amplitude. NB configuration exhibits slightly higher values during the tests performed with higher sliding frequencies, with an average force increment of 4% from F1 to F3. Concerning the effects of the torque increment, NB configuration exhibits higher values during the tests performed with higher torque values, with an average force increment of 73% from T1 to T3. In addition, it is worth noting that this difference is not significantly influenced by the sliding frequency increments.

Tables 5 and 6 list the main results of G1 tests, for NN and NB configuration respectively, in terms of steady activation force $F_{act,s}$, maximum force $F_{max,s}$, percentage difference ΔF between $F_{act,s}$ and $F_{max,s}$, coefficient of variation of the overall recorded forces cv_F and temperature increment ΔT. During the tests, NN registers $F_{act,s}$ values ranging between 3.49 and 6.87 kN, with an overall mean value of

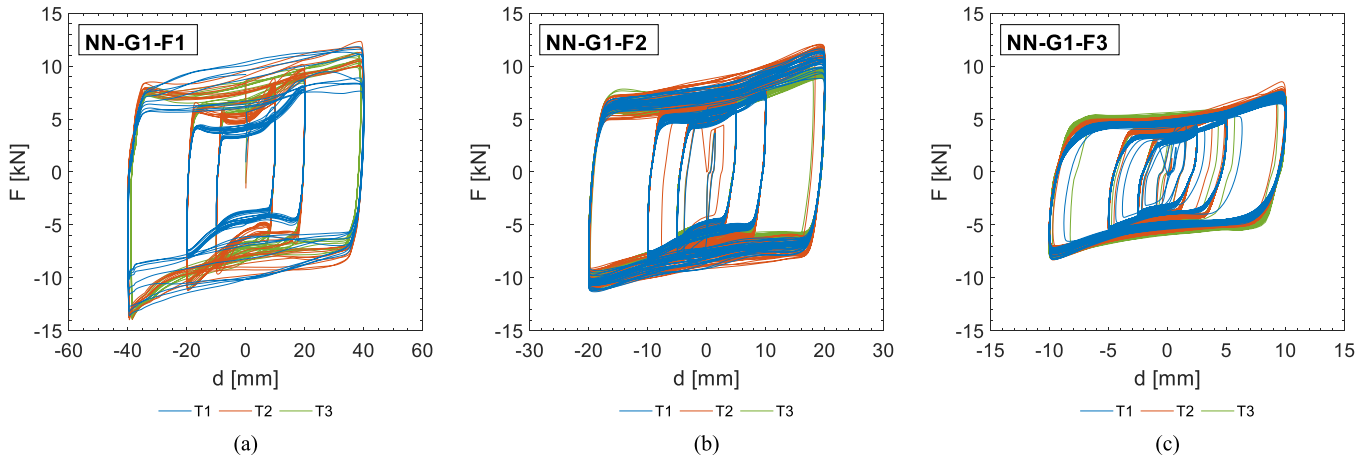

Fig. 9. G1 tests hysteresis cycles for NN configuration at a) 0.05 Hz, b) 0.50 Hz and c) 1.00 Hz oscillation frequencies.

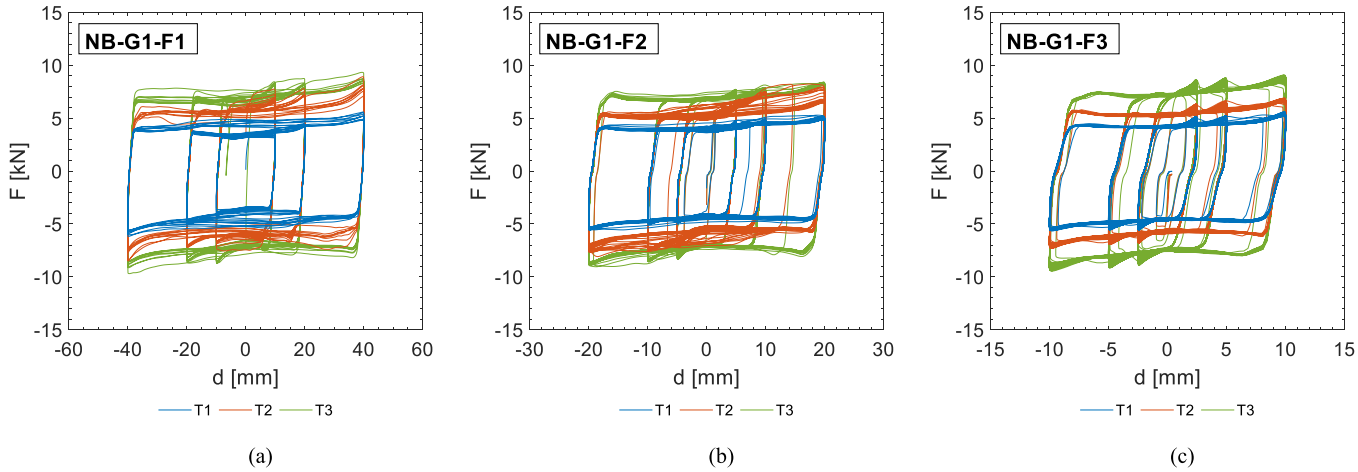

Fig. 10. G1 tests hysteresis cycles for NB configuration at a) 0.05 Hz, b) 0.50 Hz and c) 1.00 Hz oscillation frequencies.

Table 5
G1 tests main results for NN configuration.

Test tag	Torque [Nm]	$F_{act,s}$ [kN]	$F_{max,s}$ [kN]	ΔF [%]	cv_F [%]	ΔT [°C]
NN-G1-F1	40 (T1)	5.17	8.44	39	13	2.3
	60 (T2)	6.31	10.57	40	9	1.3
	100 (T3)	6.87	9.91	31	5	3.5
NN-G1-F2	40 (T1)	5.66	7.86	28	8	2.4
	60 (T2)	6.07	8.46	28	13	2.7
	100 (T3)	6.25	7.91	21	5	1.4
NN-G1-F3	40 (T1)	3.49	5.59	38	11	1.0
	60 (T2)	4.08	6.42	37	7	1.7
	100 (T3)	4.28	5.99	29	7	1.3

Table 6
G1 tests main results for NB configuration.

Test tag	Torque [Nm]	$F_{act,s}$ [kN]	$F_{max,s}$ [kN]	ΔF [%]	cv_F [%]	ΔT [°C]
NB-G1-F1	40 (T1)	3.72	4.46	16	4	0.9
	60 (T2)	5.66	7.06	20	5	0.9
	100 (T3)	6.72	8.29	19	3	1.1
NB-G1-F2	40 (T1)	3.88	4.99	22	3	1.5
	60 (T2)	5.17	6.98	26	3	1.4
	100 (T3)	6.78	8.16	17	1	2.3
NB-G1-F3	40 (T1)	3.96	5.34	26	6	1.2
	60 (T2)	5.02	6.64	24	5	1.6
	100 (T3)	6.45	8.81	27	5	2.3

5.35 kN, and $F_{max,s}$ values ranging between 5.59 and 10.57 kN, with an overall mean value of 7.91 kN. The difference between $F_{max\,,s}$ and $F_{act,s}$ values ranges between 1.66 and 4.26 kN, with an overall mean value of 2.55 kN which corresponds to an average increment of 22% from $F_{act,s}$ to $F_{max\,,s}$. NB registers F_{act} values ranging between 3.72 and 6.78 kN, with an overall mean value of 5.26 kN, and F_{max} values ranging between 4.46 and 8.81 kN, with an overall mean value of 8.81 kN. The difference between $F_{max\,,s}$ and $F_{act,s}$ values ranges between 0.73 and 2.36 kN, with an overall mean value of 1.49 kN which corresponds to an average increment of 22% from $F_{act,s}$ to $F_{max\,,s}$.

Both configurations exhibit a significant improvement in terms of activation force steadiness after the RI, registering cv_F values that average 9% and 4% for NN and NB respectively. Furthermore, it is worth noting that both configurations exhibit lower cv_F values when T3 is applied, registering cv_F values that average 6% and 3% for NN and NB respectively. Concerning the temperature increment, both configurations do not reach more than a 10% increment of room temperature, registering ΔT values lower than 4 °C for NN and NB respectively. Consequently, given the typical seismic event duration of 60 to 120 s, it is expected that the temperature increment does not influence the

overall BRFD behaviour during the real use condition.

G1 tests emphasize the differences between NN and NB configuration and confirm the outcomes of the tribological campaign [29,30]. During the steady-state stages, nickelled steel vs. nickelled steel coupling (NN) registered higher μ and coefficient of variation values than nickelled steel vs. bronze coupling (NB). As a result, it is expected to find higher force values and coefficient of variation for NN than the NB configuration. However, it is worth noting that when the torque increments, the NN configuration reaches force values similar to the NB configuration, resulting in a higher influence on torque variation than the NB configuration.

These results can be explained by the different behaviour of the friction interface associated with NN and NB and by the actual stud bolt tension reached after the application of the controlled torque. In fact, the friction between washers and plates can affect the tension transmission, leading to lower bolts' axial forces: further investigation should consider the evaluation of the actual bolt tension to determine a proper correlation between μ and the effective axial forces of bolts.

4.3. Group 2 tests (G2)

Figs. 11(a) and 11(b) show G2 tests (applied torque T3 and A3 fixed oscillations) results, for NN and NB configuration respectively, in terms of hysteresis cycles as force-displacement relationship, while Table 7 lists the registered $F_{act,s}$ and $F_{max,s}$ values as a function of the sliding frequency and their percentage difference ΔF. In both figures, the plot colours are used to highlight the increment in sliding frequency.

NN configuration exhibits a rectangular-shaped hysteresis cycle with an evident hardening effect due to the stick-slip mechanism, resulting in higher force values when reaching higher displacement amplitude, and confirming the overall behaviour registered during RI and G1 tests. During the tests, NN registers F_{act} values averaging 5.56 kN with a coefficient of variation of 14%. Concerning the effects of the frequency increment, NN configuration registers F_{act} higher values during the tests performed with higher sliding frequencies, with an average increment of 24% from 0.05 to 1.00 Hz.

NB configuration exhibits a rectangular-shaped hysteresis cycle with an evident hardening effect due to the stick-slip mechanism and a pinching effect when reversing the motion, resulting in higher force values when reaching higher displacement amplitude, differently from the overall behaviour registered during RI and G1 tests. This difference is caused by some damage experienced by the prototype stud bolts connected to the experimental setup guide at the end of the experimental campaign due to the high number of performed tests. In any case, a higher steel quality for stud bolts is suggested for further investigations.

Table 7
Force values during G2 tests for NN and NB configuration.

	NN			NB		
f [Hz]	$F_{act,s}$ [kN]	$F_{max,s}$ [kN]	ΔF [%]	$F_{act,s}$ [kN]	$F_{max,s}$ [kN]	ΔF [%]
0.05	5.28	8.93	41	6.93	9.37	26
0.10	4.83	8.36	42	6.93	9.57	28
0.15	4.97	8.49	41	6.99	9.82	29
0.20	5.04	8.42	40	6.98	9.95	30
0.25	5.40	8.34	35	7.59	9.98	24
0.50	5.62	8.68	35	7.49	10.05	25
0.75	6.41	9.36	31	7.42	10.26	28
1.00	6.97	9.55	27	7.57	10.33	27

During the tests, NB registers F_{act} values averaging 7.24 kN with a coefficient of variation of 4%. Concerning the effects of the frequency increment, NB configuration registers slightly higher values during the tests performed with higher sliding frequencies, with an average increment of 8% from 0.05 to 1.00 Hz.

Figs. 12(a) and 12 (b) show G2 test results, for NN and NB configuration respectively, in terms of hysteresis cycles as a force-velocity relationship. Both configurations register an increment of the overall force values when incrementing the sliding frequency; however, it is worth noting that forces decrease when the sliding velocity increases. This behaviour, which is more evident for NN configuration, confirms the difference between F_{act} and F_{max} values registered during G1 tests, and it is usually associated with the stick-slip behaviour.

The hysteresis cycles in terms of force-velocity of Fig. 12 are used to define a force-velocity relationship (*F-v fit* lines of Fig. 12) that will be used to define the constitutive law of friction as a function of velocity in future research. More precisely, *F-v fit* lines have been determined as the mean of values F_{act} and F_{max} for each frequency value. Both NN and NB configurations show an increment of force values between 10 and 30 mm/s with a difference between minimum and maximum values that averages 20% and 28% respectively.

It is worth noting that during G2 tests NB configuration registered slightly higher values of forces than the NN configuration, contrasting the tribological campaign findings [29,30]. In fact, NN registered lower forces despite being associated with a higher friction coefficient μ than the NB configuration. However, this behaviour can be explained considering that G2 tests have been performed using T3 torque, and during G1-T3 tests the registered $F_{act,s}$ and $F_{max,s}$ values of NB configuration are slightly higher than NN configuration. Again, this behaviour highlights the importance of evaluating the actual stud bolt tension, regardless of the application of a controlled torque, which can be affected by friction among the washers and the plates.

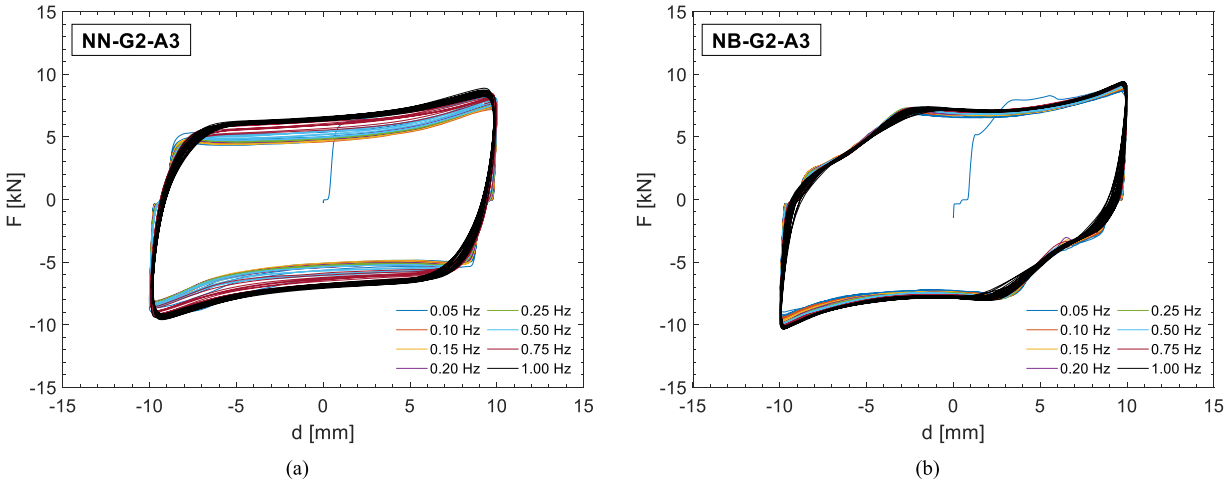

Fig. 11. G2 tests hysteresis cycles of a) NN and b) NB configurations.

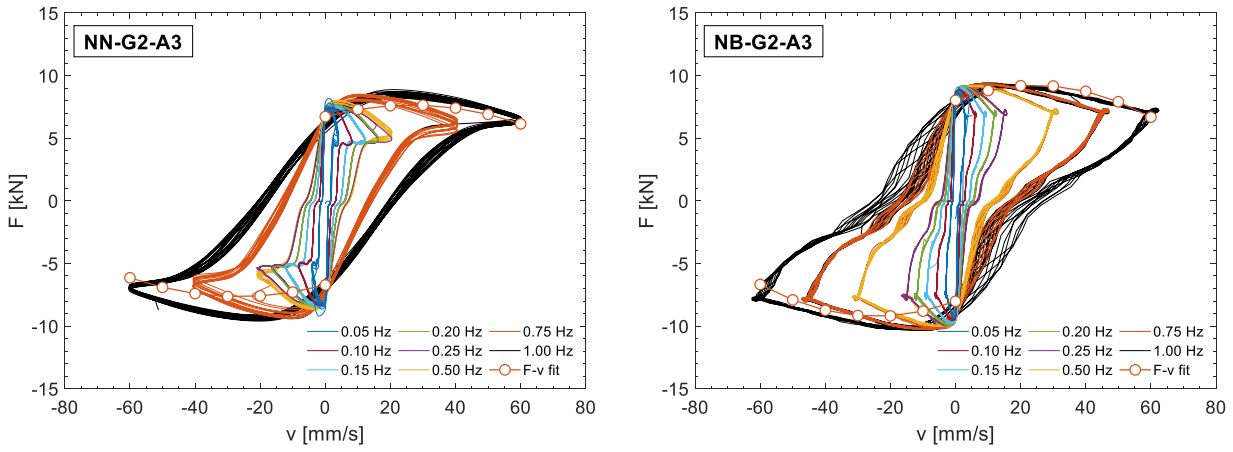

Fig. 12. G2 tests velocity hysteresis cycles of a) NN and b) NB configurations.

5. Stud bolts preload measurement investigation

The results of the experimental campaign presented above highlight the importance of the actual stud bolts' tension evaluation. To achieve that, a measurement investigation has been conducted by applying to each stud bolt four strain gauges with a resistance of 120 Ω in a full bridge configuration as shown in the specimen of Fig. 13.

The measurement system of the stud bolt tension has been calibrated applying several torque values to a stud bolt connecting two steel plates and registering the corresponsive developed bolts preload F_P. The calibration has been performed using a FERVI 0803/S210 manual torque wrench, five different torque steps from 50 to 150 Nm and applying two different torque increment methodologies. In the first one, the increment of torque was applied without unloading the connection at each new step, while in the second one, the increment of torque was applied by unloading the connection at each step. Fig. 14 shows the calibration results in terms of torque and bolts preload relationship. When the torque increment is applied without unloading the connection at each new step, the recorded F_P values roughly follow the expected linear increment and the torque coefficient [41] k_m averages 0.32 with a coefficient of variation equal to 17%. On the contrary, when the torque increment is applied unloading the connection at each new step, the recorded F_P values better follow the expected linear increment and the torque coefficient [41] k_m averages 0.20 with a coefficient of variation equal to 6%. In addition, much higher F_P values are obtained by unloading the connection before the torque increment application.

The results of the calibration suggest that to develop a more predictable bolt tension during the tests, the application of the torque increment should be executed by unloading the bolted connection at each increment step.

Additional G1 tests have been performed at the frequency of 0.05 Hz, torque 100 Nm and using the instrumented stud bolts. The results are reported in Fig. 15 in terms of recorded hysteresis cycles and developed bolts preload F_P for both NN and NB configurations.

The recorded hysteresis cycles (see Fig. 15(a)) have a similar shape to the ones previously recorded; however, while NB configuration reaches force values similar to the previous ones, NN configuration registers force values higher than the previous ones. This difference can be explained by the F_P values developed by NN during this test, which average 24.18 kN, and almost doubles the F_P values developed by NB configuration, which averages 12.53 kN. Considering the recorded sliding forces and bolts' preload forces, the friction coefficients associated with NN and NB configuration are estimated to equal 0.63 and 0.52 respectively. These results do not significantly differ from the findings of the previous tribological campaign [29,30].

Fig. 13. Stud bolt with strain gauges installed.

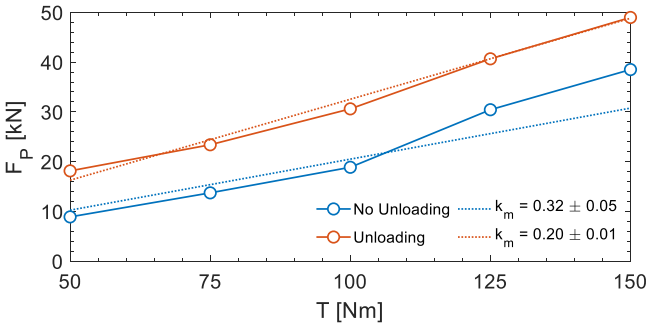

Fig. 14. Strain gauges calibration results.

The adopted torque technique did not produce the same F_P values in the investigated configurations, and this difference can be responsible for the peculiar results of the experimental campaign. In addition to that, it is worth noting that during the tests F_P values (see Fig. 15(b)) are not constant, but they oscillate following the oscillations of the imposed displacements. Unfortunately, after 420 s of NB configuration testing, the strain gauges of the bolts broke because the sliding motion of the plates around the stud bolts cut the strain gauge wires. This measurement system was revealed to be not reliable enough and a better solution has to be sought for future tests.

6. Conclusions

The present work shows the results of the preliminary tests performed on the prototype of a novel friction damper with two different mating interfaces (NN and NB configurations). The main findings in terms of transition time, hysteresis cycle steadiness and effects of torque and sliding frequency increment are listed below:

- NN registers higher t_{tr} and cv_F values than NB configuration, both highlighting the necessity of a proper running-in stage (RI) to develop a steadier hysteresis cycle during the real use conditions.

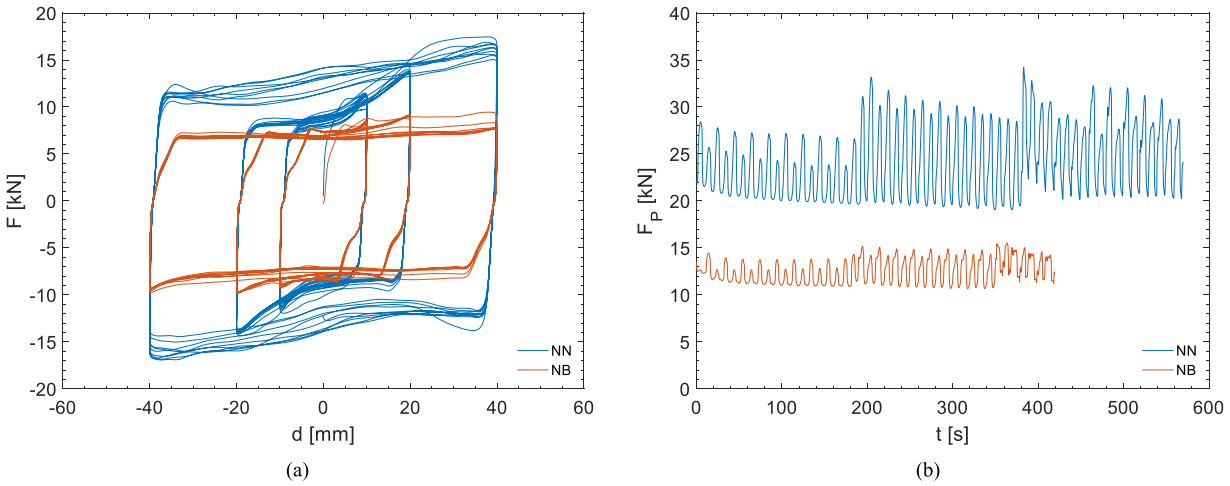

Fig. 15. Additional test results in terms of a) hysteresis cycles and b) bolts load of NN and NB configurations.

- Both NN and NB configurations registered lower cv_F values after RI tests, especially when subjected to higher stud bolts' torque values, highlighting the improvement in terms of steadiness of hysteresis cycles after the RI.
- NN registered similar force values with the increment of stud bolts' torque value and lower force values with the increment of the sliding frequency, showing a coefficient of friction highly influenced by both bolts preload and sliding velocity. On the contrary, NB registered higher force values with the increment of the stud bolts torque value and similar force values with the increment of the sliding frequency, showing a coefficient of friction modestly influenced by both bolts preload and sliding velocity.
- The measurement investigation of the bolt tension highlighted the need for a proper torquing technique to develop a reliable stud bolt preload and the need for additional sensors, preferably embedded into the stud bolt, to measure and control the actual bolt preload.

The results of the preliminary tests allow the assessment of the selected NN and NB configurations in terms of stable and reliable hysteresis cycles for the BRFD in development, which is the main goal of this research program. Additionally, the experimental findings allow the development of preliminary numerical constitutive models to define the overall behaviour of the proposed device. Since NN and NB configurations have shown different tribological behaviours, different constitutive models will be implemented for a sound numerical calibration and prevision tool development of both cases.

The performed tests have successfully highlighted a very promising behaviour of the BRFD thanks to both good damping capacity and reliability of the hysteresis cycles, especially for the NB configuration, in here considered the most interesting. In fact, despite the development of lower friction coefficient values than NN, the steadiness of the hysteresis cycles is considered by the authors more reliable and then preferable.

Future developments will concern the investigation of BRFD bidirectional behaviour, and further experimental tests will be performed soon considering both displacement components. Moreover, several sensors will be installed to detect the real stud bolts' axial tension and assess the effective influence of the bolts' preload.

CRediT authorship contribution statement

Eleonora Grossi: Writing – original draft, Visualization, Software, Investigation, Formal analysis, Data curation, Conceptualization. **Matteo Zerbin:** Writing – review & editing, Validation, Supervision, Methodology. **Alessandra Aprile:** Writing – review & editing, Validation, Supervision, Resources, Project administration, Methodology, Funding acquisition, Conceptualization. **Paolo Livieri:** Validation, Supervision, Resources, Methodology, Investigation.

Declaration of Competing Interest

The authors declare the following financial interests/personal relationships which may be considered as potential competing interests Eleonora Grossi has patent #102020000013738/2021 issued to Italian Patent and Trademark Oce, Ministry of Economic Development. Alessandra Aprile has patent #102020000013738/2021 issued to Italian Patent and Trademark Oce, Ministry of Economic Development. Matteo Zerbin has patent #102020000013738/2021 issued to Italian Patent and Trademark Oce, Ministry of Economic Development.

Data Availability

Data will be made available on request.

Acknowledgements

The authors wish to acknowledge the support provided by the University of Ferrara: "Bidirectional Friction Links for Seismic Retrofit of Existing Precast RC Structures (FAR2078914)", "A friction damper for seismic retrofit of precast RC structures (FAR2151302)", "Experimental testing of innovative friction dampers for seismic retrofit of precast RC structures (FAR22718675)". The authors wish also to acknowledge the support provided by FIRD funding from the Engineering Department of the University of Ferrara, year 2022: "Mechanical and tribological testing of a novel damping device for seismic risk mitigation of industrial buildings (2022-FAR.L-FIRD_DE_AA_001)".

References

[1] Grossi E, Zerbin M, Aprile A. Advanced techniques for pilotis RC frames seismic retrofit: performance comparison for a strategic building case study. Buildings 2020;10:149. https://doi.org/10.3390/buildings10090149.
[2] Zerbin M, Aprile A. Sustainable retrofit design of RC frames evaluated for different seismic demand. Earthq Struct 2015;9:1337–53. https://doi.org/10.12989/EAS.2015.9.6.1337.
[3] Christopoulos C, Filatrault A. Principles of Passive Supplemental Damping and Seismic Isolation. Pavia, Italy: IUSS Press; 2006.
[4] Pall AS, Marsh C. Seismic response of friction damped braced frames. J Struct Div 1982;108:1313–23.
[5] Jaisee S, Yue F, Ooi YH. A state-of-the-art review on passive friction dampers and their applications. Eng Struct 2021;235:112022. https://doi.org/10.1016/j.engstruct.2021.112022.
[6] International Federation for Structural Concrete. Seismic design of precast concrete building structures: state-of-art report. vol. 27. Lausanne: fib; 2003.
[7] Toniolo G. Safecast project: european research on seismic behaviour of the connections of precast structures. Proceedings of the 4th International Conference

on Computational Methods in Structural Dynamics and Earthquake Engineering (COMPDYN 2013), Athens: Institute of Structural Analysis and Antiseismic Research School of Civil Engineering National Technical University of Athens (NTUA) Greece; 2014, p. 1482–1493. https://doi.org/10.7712/120113.4609.C1430.
[8] Casotto C, Silva V, Crowley H, Nascimbene R, Pinho R. Seismic fragility of Italian RC precast industrial structures. Eng Struct 2015;94. https://doi.org/10.1016/j.engstruct.2015.02.034.
[9] Batalha N, Rodrigues H, Varum H. Seismic performance of RC precast industrial buildings—learning with the past earthquakes. Innov Infrastruct Solut 2019;4. https://doi.org/10.1007/s41062-018-0191-y.
[10] Sousa R, Batalha N, Silva V, Rodrigues H. Seismic fragility functions for Portuguese RC precast buildings. Bull Earthq Eng 2021;19:6573–90. https://doi.org/10.1007/s10518-020-01007-7.
[11] Constantinou MC, Tsopelas P, Hammel W, Sigaher AN. Toggle-brace-damper seismic energy dissipation systems. J Struct Eng 2001;127. https://doi.org/10.1061/(ASCE)0733-9445(2001)127:2(105).
[12] Martínez-Rueda JE. On the evolution of energy dissipation devices for seismic design. Earthq Spectra 2002;18. https://doi.org/10.1193/1.1494434.
[13] Soong TT, Spencer BF. Supplemental energy dissipation: state-of-the-art and state-of-the-practice. Eng Struct 2002;24. https://doi.org/10.1016/S0141-0296(01)00092-X.
[14] Barzegar V, Laflamme S, Downey A, Li M, Hu C. Numerical evaluation of a novel passive variable friction damper for vibration mitigation. Eng Struct 2020;220. https://doi.org/10.1016/j.engstruct.2020.110920.
[15] Wang Y, Zhou Z, Xie Q, Huang L. Theoretical analysis and experimental investigation of hysteretic performance of self-centering variable friction damper braces. Eng Struct 2020;217. https://doi.org/10.1016/j.engstruct.2020.110779.
[16] Dal Lago B, Naveed M, Lamperti Tornaghi M. Tension-only ideal dissipative bracing for the seismic retrofit of precast industrial buildings. Bull Earthq Eng 2021;19:4503–32. https://doi.org/10.1007/s10518-021-01130-z.
[17] Latour M, D'Aniello M, Zimbru M, Rizzano G, Piluso V, Landolfo R. Removable friction dampers for low-damage steel beam-to-column joints. Soil Dyn Earthq Eng 2018;115. https://doi.org/10.1016/j.soildyn.2018.08.002.
[18] Francavilla AB, Latour M, Piluso V, Rizzano G. Design criteria for beam-to-column connections equipped with friction devices. J Constr Steel Res 2020;172. https://doi.org/10.1016/j.jcsr.2020.106240.
[19] Kim H-J, Christopoulos C. Friction damped posttensioned self-centering steel moment-resisting frames. J Struct Eng 2008;134. https://doi.org/10.1061/(ASCE)0733-9445(2008)134:11(1768).
[20] Eldin MN, Dereje AJ, Kim J. Seismic retrofit of RC buildings using self-centering PC frames with friction-dampers. Eng Struct 2020;208. https://doi.org/10.1016/j.engstruct.2019.109925.
[21] Huang L, Zhou Z, Huang X, Wang Y. Variable friction damped self-centering precast concrete beam–column connections with hidden corbels: Experimental investigation and theoretical analysis. Eng Struct 2020;206:110150. https://doi.org/10.1016/j.engstruct.2019.110150.
[22] Valente M. Improving the seismic performance of precast buildings using dissipative devices. Procedia Eng, vol. 54, Elsevier Ltd; 2013, p. 795–804. https://doi.org/10.1016/j.proeng.2013.03.073.
[23] Colajanni P, La Mendola L, Monaco A, Pagnotta S. Design of RC joints equipped with hybrid trussed beams and friction dampers. Eng Struct 2021;227. https://doi.org/10.1016/j.engstruct.2020.111442.
[24] Martinelli P, Mulas MG. An innovative passive control technique for industrial precast frames. Eng Struct 2010;32. https://doi.org/10.1016/j.engstruct.2009.12.038.
[25] Belleri A, Marini A, Riva P, Nascimbene R. Dissipating and re-centring devices for portal-frame precast structures. Eng Struct 2017;150. https://doi.org/10.1016/j.engstruct.2017.07.072.
[26] Pollini AV, Buratti N, Mazzotti C. Behavior factor of concrete portal frames with dissipative devices based on carbon-wrapped steel tubes. Bull Earthq Eng 2021;19:553–78. https://doi.org/10.1007/s10518-020-00977-y.
[27] Huang W, Hu G, Miao X, Liu X, Xie H. Seismic performance of concrete-filled steel tube devices for precast concrete beam-column connections. J Mech Mater Struct 2021;16:63–88. https://doi.org/10.2140/JOMMS.2021.16.63.
[28] Bressanelli ME, Bosio M, Belleri A, Riva P, Biagiotti P. Crescent-moon beam-to-column connection for precast industrial buildings. Front Built Environ 2021;7. https://doi.org/10.3389/fbuil.2021.645497.
[29] Grossi E, Aprile A, Zerbin M. Tribological investigation on metal mating surfaces to explore real use conditions of a novel friction damper for seismic applications. Eng Struct 2023;278:115473. https://doi.org/10.1016/j.engstruct.2022.115473.
[30] Grossi E, Baroni E, Aprile A, Fortini A, Zerbin M, Merlin M. Tribological behavior of structural steel with different surface finishing and treatments for a novel seismic damper. Coatings 2023;13:135. https://doi.org/10.3390/coatings13010135.
[31] CEN. Anti-seismic devices (UNI EN 15129:2018). 2018.
[32] Grigorian CE, Yang TS, Popov EP. Slotted bolted connection energy dissipators. Earthq Spectra 1993;9. https://doi.org/10.1193/1.1585726.
[33] Latour M, Piluso V, Rizzano G. Experimental analysis on friction materials for supplemental damping devices. Constr Build Mater 2014;65. https://doi.org/10.1016/j.conbuildmat.2014.04.092.
[34] De Serra A. Adeguamento sismico di uno stabilimento produttivo prefabbricato in c.a. mediante dissipatori innovativi DoubleDamp: zona produzione. Master Thesis. University of Ferrara, 2023.
[35] D'Agostini S. Adeguamento sismico di uno stabilimento produttivo prefabbricato in c.a. mediante dissipatori innovativi DoubleDamp: zona cantina. Master Thesis. University of Ferrara, 2023.
[36] CEN. Hot rolled products of structural steels - Part 1: General technical delivery conditions (UNI EN 10025–1:2005). 2015.
[37] CEN. High-strength structural bolting assemblies for preloading - Part 1: General requirements (UNI EN 14399–1:2015). 2015.
[38] Morgen BG, Kurama YC. Characterization of two friction interfaces for use in seismic damper applications. Mater Struct 2009;42. https://doi.org/10.1617/s11527-008-9365-y.
[39] Chanchi Golondrino JC, MacRae GA, Chase JG, Rodgers GW, Clifton GC. Seismic behaviour of symmetric friction connections for steel buildings. Eng Struct 2020;224. https://doi.org/10.1016/j.engstruct.2020.111200.
[40] The MathWorks Inc, MU. MATLAB, Version R2021a 2021.
[41] CEN. Execution of steel structures and aluminium structures - Part 2: Technical requirements for steel structures (EN 1090–2:2018). 2018.